ADVANCED ENERGY MATERIALS
www.advenergymat.de

Can Nanosecond Laser Achieve High-Performance Perovskite Solar Modules with Aperture Area Efficiency Over 21%?

Yanyan Gao, Chong Liu, Yi Xie, Rilang Guo, Xuqi Zhong, Huanxin Ju, Li Qin, Peng Jia, Shaohang Wu, Ruud E. I. Schropp, and Yaohua Mai**

Overcoming cell-to-module (CTM) efficiency losses is indispensable to realize large-area high-efficiency perovskite photovoltaic devices for commercialization. Laser scribing technology is used to fabricate perovskite modules, but it does not seem to solve the problem of high-quality interconnection and high geometric filling factor (GFF), which are the prerequisites for overcoming CTM losses. In reality, what kind of laser technology is needed to fabricate high-efficiency perovskite solar modules is still an open question. Herein, this work demonstrates that a nanosecond pulse laser is able to deliver a reduced heat-affected zone due to the small thermal diffusion coefficient (D_t) of perovskite material, contributing to the accomplishment of a high GFF of up to 95.5%. In addition, the monolithic interconnection quality is improved by finely lifting off the capping layers on indium tin oxide and identifying the residue within the scribed area. As a result, a certified aperture area efficiency of 21.07% under standard 100 mW cm^{-2} AM1.5G illumination is achieved with a high photovoltaic fill factor exceeding 80%. The present study provides guidance in overcoming key CTM efficiency losses in perovskite photovoltaic technology.

1. Introduction

Perovskite photovoltaic technology is attracting increasing attention in recent years as the certified power conversion efficiency (PCE) of small-area laboratory perovskite solar cells (PSCs) has reached 25.7%,[1–4] which is at a level that is comparable to the state-of-the-art silicon solar cells. Presently, the potential for mass production of perovskite solar modules (PSMs) is being intensively explored, and the PCE is steadily improving (Figure S1, Supporting Information). The development of high throughput manufacturing technologies is crucial to fulfilling the prerequisites of mass production of photovoltaic panels with short tact times and good reproducibility. High precision, fine resolution laser scribing technology has the advantages of low cost, fast operating speed, and small area loss, making it far superior to other structuring methods to realize commercial-scale production of high-performance thin film solar cells.[5]

The laser photons are absorbed by the solar cell materials and their energy is first absorbed by free electrons, and then transferred to the lattice, leading to material gasification.[6] Thus, the longer the pulse duration, that is, the more the laser pulse exceeds the duration of the electron-lattice interaction, the more likely it is to generate a larger heat-affected zone (HAZ), as excess energy diffuses into the material in the form of lattice vibrations. Therefore, lasers generating ultrashort (picosecond or femtosecond) pulses are more attractive for processing devices that are sensitive to the presence of a HAZ rather than the short pulse laser (nanosecond). Organic–inorganic hybrid PSCs have been developed for over 10 years, and have reached the stage of industrialization.[7] However, in-depth research on laser processing for module manufacturing is lacking. For instance, the question of whether picosecond (ps) or femtosecond (fs) lasers are critically required to fabricate a high geometric filling factor (GFF) and photovoltaic performance PSMs has not been studied systematically.

Ballif et al. first reported laser-scribed PSMs in 2015 with a GFF of 84% by using a nanosecond (ns) pulse laser.[8] In 2021, Huang et al. gained an active area PCE of 20.4% for a PSM by utilizing a femtosecond (fs) pulse laser, starting from a PCE of PSC of 23.35%.[9] Recently, an active area PCE of 21.4% was achieved by Nazeeruddin et al. for their PSMs, while the GFF was as high as 90.2%.[10] Seok et al. achieved an aperture area efficiency of 20.4% and a GFF of 94.36% by using a ps pulse laser.[11] It can be concluded that the improvement of aperture area PCE's of PSMs still suffers from considerable cell-to-module (CTM) efficiency losses and/or low GFF even when

---

Y. Gao, C. Liu, Y. Xie, R. Guo, X. Zhong, S. Wu, R. E. I. Schropp, Y. Mai
Institute of New Energy Technology
College of Information Science and Technology
Jinan University
Guangzhou 510632, China
E-mail: wushaohang@jnu.edu.cn; yaohuamai@jnu.edu.cn

Y. Gao, C. Liu, Y. Xie, R. Guo, X. Zhong, S. Wu, Y. Mai
Key Laboratory of New Semiconductors and Devices of Guangdong Higher Education Institutes
Jinan University
Guangzhou 510632, China

H. Ju
PHI China Analytical Laboratory
CoreTech Integrated Limited
402 Yinfu Road, Nanjing 211111, China

L. Qin, P. Jia
Key Laboratory of Luminescence and Application
Changchun Institute of Optics
Fine Mechanics and Physics
Chinese Academy of Sciences
Changchun 130033, China

The ORCID identification number(s) for the author(s) of this article can be found under https://doi.org/10.1002/aenm.202202287.

DOI: 10.1002/aenm.202202287

ultrashort pulse laser technology is applied.[12] In order to investigate the factors affecting the sub-cell separation and module interconnection for PSMs, systematic research on laser scribing technologies is needed.

In this work, the carrier recombination risk associated with the laser scribing process is analyzed. We find that ns pulse laser scribing of the perovskite thin film is able to deliver a very small HAZ, which was verified by model simulations and experiments. Micro-Raman spectroscopy was used to identify the residue within the scribed area, and photoluminescence mapping was used to determine the extent of the HAZ. As a result, the laser pulse power (E_p) was optimized by monitoring the sub-cell interconnection quality and the HAZ. Finally, we achieved a certified aperture efficiency of 21.07% with a GFF of 95.5%, which are both among the highest reported values for aperture area PCE and GFF so far.

2. Results and Discussion

Here, we fabricate inverted PSCs with the structure of indium tin oxide (ITO)/poly[bis(4-phenyl)(2,5,6-trimethylphenyl)amine (PTAA)/Al_2O_3/$Cs_{0.05}(FA_{0.9}MA_{0.1})_{0.95}Pb(I_{0.9}Br_{0.1})_3$/$C_{60}$/$SnO_2$/Ag, as shown in the cross-sectional scanning electron microscope (SEM) image in **Figure 1**a. All of the thin films have a well-defined layer structure, and the PSC statistics demonstrate a narrow efficiency distribution, indicating a high manufacturing reproducibility (Figure S2, Supporting Information). The best performing PSC, with an area of 0.09 cm^2 has a PCE of 22.16%, a J_{SC} of 23.23 mA cm^{-2}, a V_{OC} of 1.15 V, and a FF of 0.83. The external quantum efficiency (EQE) spectrum shows an integrated J_{SC} of 22.58 mA cm^{-2} (Figure S3, Supporting Information), which is fairly close to the *J*–*V* results (deviation less than 5%). In addition, the PSC shows a negligible hysteresis effect with an H-index value of 3.65% (Figure 1b).

To fabricate a module, the solar cells need to be divided into an array of sub-cells that are interconnected in series to obtain a high voltage and low photocurrent device with the aim of reducing resistive losses.[13] In this work, the transparent ITO front contact layer-based PSC facilitates induced ablation of the entire multilayer structure through the glass side while preserving the ITO. Compared with patterning from the film side (defined as direct ablation), the induced ablation provides a series of advantages including sharp-edged patterns, smaller HAZs, and avoidance of screening by the plume.[6] The laser processing consists of three sequential scribing steps, that is, P1, P2, and P3 (Figure 1c). P1 aims to separate the ITO film into strips to define the individual sub-cells deposited over the scribed ITO film. We used a 30 ns laser with a wavelength of 1064 nm to scribe P1 because a wide band gap ITO has free carrier absorption in the near-infrared region (Figure S4, Supporting Information). Typically, the high pulse-to-pulse overlap is used in P1 patterning to obtain clean and smooth scribe line valleys (Figure S5, Supporting Information). In the P2 patterning step, the perovskite layer, as well as other functional layers (charge transport layers and buffer layers) are removed to construct interconnections between the sub-cells. In the P3 step, the top electrode is removed along with all other layers except the ITO, to exclude shunting of adjacent sub-cells of the device. A 0.4 ns green laser with a wavelength of 532 nm was used for scribing P2 and P3 since this wavelength is optimally absorbed in the perovskite layer (Figure S4, Supporting Information). We calculated the light absorption of the 532 nm laser beam within the solar cell by finite element analysis using

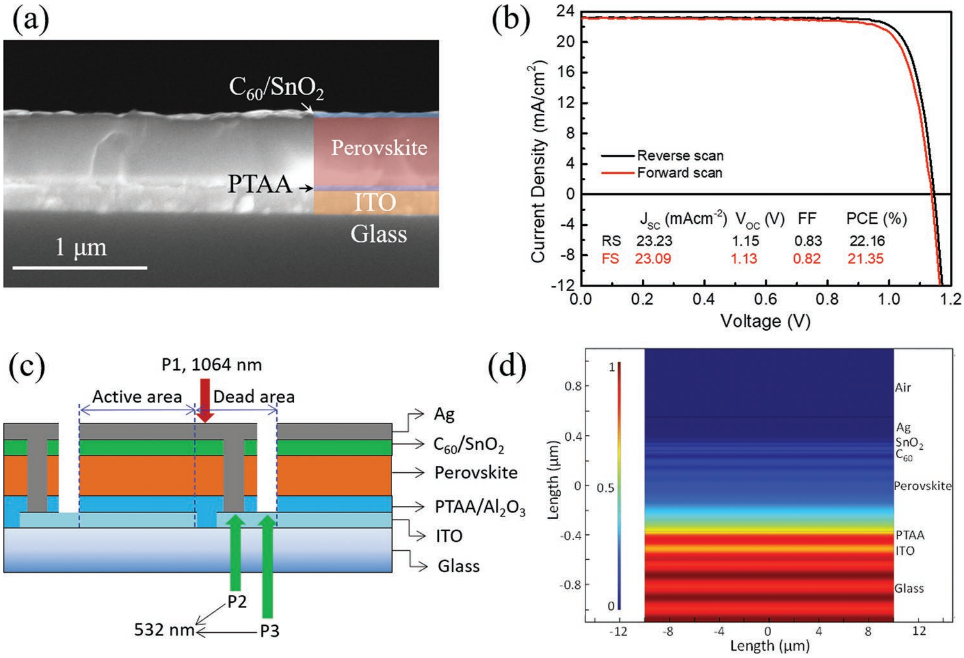

Figure 1. a) Cross-sectional SEM image of the PSC. b) Forward and reverse *J*–*V* curves of the champion PSC. c) Schematic illustration of the monolithic interconnection of the PSM. d) Multiple physical field coupling calculation of PSC for a laser beam with a wavelength of 532 nm incident from the glass side.

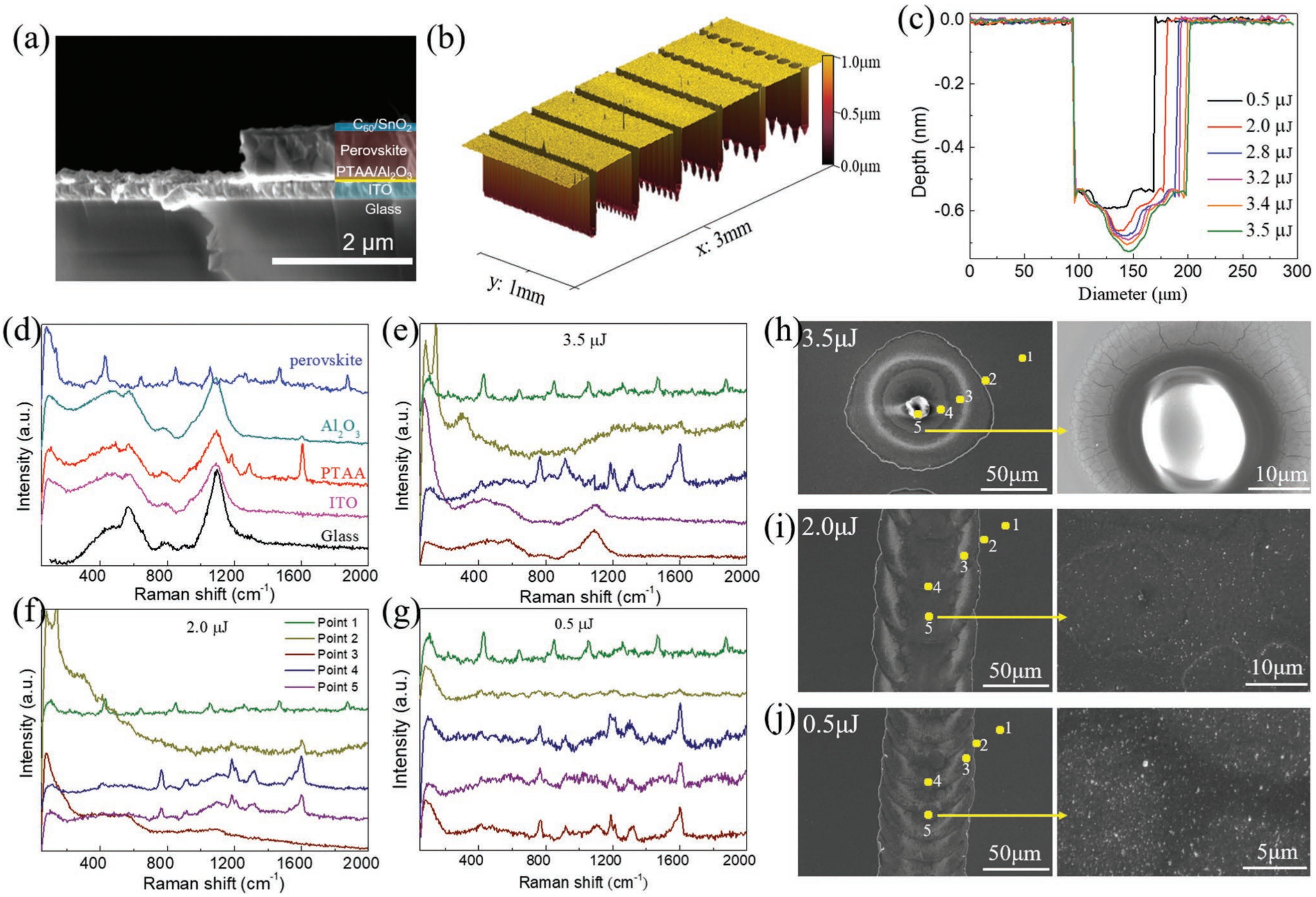

Figure 2. a) Cross-section SEM images of the P2 scribe line. b,c) Microscope 3D image and the as-extracted outline curves of the P2 scribe line patterned with different E_p. d) Raman shift spectra of glass, ITO, PTAA, Al_2O_3, and perovskite material; e–g) Raman shift spectra of five points selected outside the center spot produced at different E_p. h–j) Surface SEM images of the P2 scribe line produced at different E_p, along with different zoomed-in views.

Comsol multiphysics-RF module (Figure 1d). The thermal properties of the materials of which the PSC is constructed are listed in Table S1, Supporting Information. It is observed that the maximum attenuation region of |E| lies in the perovskite layer, which means that most of the laser energy is absorbed by the perovskite material (Figure 1d and Figure S6, Supporting Information). As the ITO layer also has an absorption of the 532 nm laser light, proportional to the laser pulse energy (E_p), the E_p should be carefully optimized to avoid damage to the underlying ITO.

During the P2 pattern, the 532 nm laser beam passes through the ITO and is absorbed by the perovskite material, resulting in a fast temperature rise to evaporation of the material, which in turn produces local strain that causes lift off of the capping layers. It is important that the P2 scribe is carefully controlled to form a valley with no residue so that an ideal metal-ITO ohmic contact is created later.[14] We adjusted the E_p of the laser pulses from 0.5 to 3.5 μJ, and the corresponding 3D micrograph images of these P2 scribes can be seen in **Figure 2**b. We found that both the width and depth of the scribe tend to get larger with increasing E_p (Figure 2c and Figure S7, Supporting Information). In addition, to reach the maximum depth even by low energy pulses, the laser source is operated at a higher repetition rate (f_p) to form appropriate pulse-to-pulse overlap.

In order to optimize the laser pulse energy, we employed micro-Raman spectroscopy with high resolution (<1 μm) and high surface sensitivity (≈10 nm) to detect residual components at specific positions of the P2 scribe.[15] As can be seen in Figure 2c, the valleys of the scribes are not flat, and they get deeper at positions closer to the center of the laser spot. Five points are selected outside of the spot center, and the Raman shift spectra are depicted in Figure 2e–g. The Raman shift spectra of each material (i.e., perovskite, Al_2O_3, PTAA, ITO, and glass) as used in the PSM have been recorded beforehand (Figure 2d). The ITO exhibits no characteristic peak from 50 to 2000 cm^{-1}, which makes the layer unsuitable for analysis by micro-Raman spectroscopy. Fortunately, the ultrathin (8 nm) PTAA layer on top of the ITO has distinguishable characteristic peaks at 1605.2 cm^{-1}, while the peak almost disappears when covered by an Al_2O_3 nanoparticle layer, which is favorable for accurate location of the scribing depth. The perovskite material shows a series of peaks, where the peaks at 60 and 100 cm^{-1} are associated with the bending and stretching mode of the Pb—I bond.[16] At a laser pulse energy of E_p = 3.5 μJ, the ITO layer is clearly punctured at point 4 and point 5, according to the SEM image and the Raman shift spectra (Figure 2e,h). The Raman shift spectra of points 2, 3, and 4 all show the characteristic peak of PTAA, but it disappears at point 5 with an E_p of 2 µJ, indicating that the materials on top of ITO at point 5 are almost completely removed (Figure 2f,i and Figure S8, Supporting Information). The cross-section and surface SEM images in Figure 2a and Figure S8, Supporting Information, show that some residue still exists because of the Gaussian distribution of the laser power over the spot size, which results in insufficient pulse power at the spot overlaps. Indeed, since the materials on top of the ITO have been almost completely removed at point 5, the scribe line prepared by 2 µJ is expected to facilitate a sufficiently low contact resistance between the metal and the ITO. In contrast, the materials on top of the ITO cannot be well removed when the E_p is 0.5 µJ (Figure 2g,j), which will inevitably increase the contact resistance.

The HAZ related to the P2 scribe (HAZ-P2) is determined by the laser spot spatial power profile and its thermal penetration depth (TPD), as shown schematically in the diagram of the scribe formation mechanism in Figure S9, Supporting Information. The Gaussian distribution of the laser power leads to locations in the beam where the energy is below the ablation threshold of vaporization of the materials, resulting in a material that is not removed but just being heated. The TPD can be estimated as follows:[6]

$$L_{th} = 2\sqrt{D_t \times \tau_p} = 2\sqrt{\frac{k\tau_p}{\rho c}} \tag{1}$$

where D_t is the thermal diffusion coefficient, τ_p is the pulse duration, k is the thermal conductivity, ρ is the density, and c is the specific heat capacity. According to literature reports, the D_t at room temperature of perovskite material is generally nearly two orders of magnitude smaller than that of other established thin film materials.[17,18] For instance, the D_t of $MAPbI_3$ is about 0.28 mm s^{-1}, while the D_t of GaAs is about 26 mm s^{-1}. As a result, the calculated width of the TPD in perovskite materials produced by a 0.4-ns pulse laser is as small as 21 nm, which is negligible in comparison to the width of the scribe line. Thus, the HAZ-P2 of the perovskite thin film is mainly determined by the profile of the laser beam rather than the pulse duration. A laser spot with a flattop beam intensity distribution thus not only causes only little residue but also reduces the ITO damage and HAZ (Figure S10, Supporting Information).[19]

In this work, the HAZ-P2 was identified by PL mapping characterization. As can be seen in **Figure 3**a, the gradual decrease in PL intensity outside the single laser spot indicates that the perovskite materials undergo changes in properties as a result of exposure to high temperatures. The HAZ expands as the overlap of spots gets larger, due to the accumulation of pulse energy within the scribe line, as well as in the region surrounding the scribe (Figure 3a–c). Scribing a continuous line requires removing the materials within the line as much as possible, leading to a trade-off between spot overlap and HAZ. Micro-zone X-ray photoelectron spectroscopy (XPS) was performed to investigate the component variation of the perovskite materials in the HAZ-P2. The appearance of two peaks, 136.8 and 141.6 cm^{-1}, shows that the perovskite material was partially decomposed into an elemental lead (Pb^0) after laser processing (Figure S11, Supporting Information).[20] We performed thermal modeling using the Comsol multiphysics-RF module of the glass/ITO/PTAA/perovskite device scribed at different E_p. At $E_p = 3.5$ µJ, the temperature of the underlying ITO at the center of the laser spot can reach temperatures close to 1000 °C (Figure 3d,g), leading to potential damage to the ITO, while the temperature increases to only about 500 °C when the E_p is 2.0 µJ (Figure 3e). Although 500 °C is slightly beyond the temperature tolerance limit of ITO, the ITO cools down in just 0.1 ms, which is so quickly that the damage is negligible (Figure 3h). On the other hand, the perovskite material at $E_p = 2.0$ µJ reaches a temperature exceeding 1100 °C, which is sufficient for ablation (Figure 3e). At the lowest E_p of 0.5 µJ, the temperature only reaches 500 °C (Figure 3h), which inevitably leads to inadequate ablation. In our simulations of HAZ-P2, we also compared the diameter of the laser spot with the width of the region that is heated by the laser beam. In this work, the diameter of the laser spot is about 100 µm, and thus, the width of HAZ-P2 is calculated to be about 20 µm in the $E_p = 2.0$ µJ condition. This result is consistent with the observed width of the HAZ in the PL mapping image. A similar procedure was applied to optimize the P3 scribe. Different from the P2, the perovskite materials in the P3 groove do not need to be cleared completely. Moreover, the suitable pulse-to-pulse overlap is assumed to gain the smooth edge of P3 (Figure S12, Supporting Information). The HAZ-P3 was identified in the SEM image using the local changes in electrode conductivity. The optimized E_p is 2.8 µJ at which the HAZ-P3 is about 12 µm (Figure S13, Supporting Information). The narrow width of HAZ helps to shorten the spacing between the P1, P2, and P3 scribes, thus reducing the dead area and increasing the GFF.

After the optimization of the laser parameters for the P1, P2, and P3 scribes, an optimized narrow dead area was obtained, as displayed in the microscope image of **Figure 4**g. The total width of the dead area (W_d) was narrowed down to 270 µm, while the subcell width was kept at 6 mm, resulting in a GFF of 95.5%. Subsequently, we compared the photovoltaic performance of PSMs fabricated with P2 scribes at different laser E_p. At the condition of $E_p = 0.5$ µJ, a large HAZ leads to a drop in device current (I), and the metallic Pb^0 residue is responsible for the leakage losses that limit the device open circuit voltage (V_{OC}) (Figure 4a,b). Although the highest V_{OC} was obtained at $E_p = 3.5$ µJ, the damage of the ITO under this condition led to an increase in series resistance (R_s), affecting the fill factor (FF) of the modules (Figure 4b,c). Therefore, the PSMs patterned at $E_p = 2.0$ µJ showed the best photovoltaic performance (Figure 4d). To further quantify how different laser powers affect the interconnection quality and the module parameters, we measured the I–V curves of a typical device under various illumination intensities (Figure S14, Supporting Information). The I–V curves were fitted using a common literature model,[26,27] and the obtained parameters are listed in Table S2, Supporting Information. The R_{sh} of the PSM processed at $E_p = 0.5$ µJ is 2027.7 Ω, which is the lowest, and the R_s of the PSM scribed at $E_p = 3.5$ µJ is 13.38 Ω, which is the highest. The PSM patterned at $E_p = 2.0$ µJ has the best overall performance, with an R_s of 0.2 Ω and an R_{sh} of 2759.3 Ω.

We sent our champion PSM (Figure 4e) to the Chinese national PV industry measurement and testing center (NPVM)

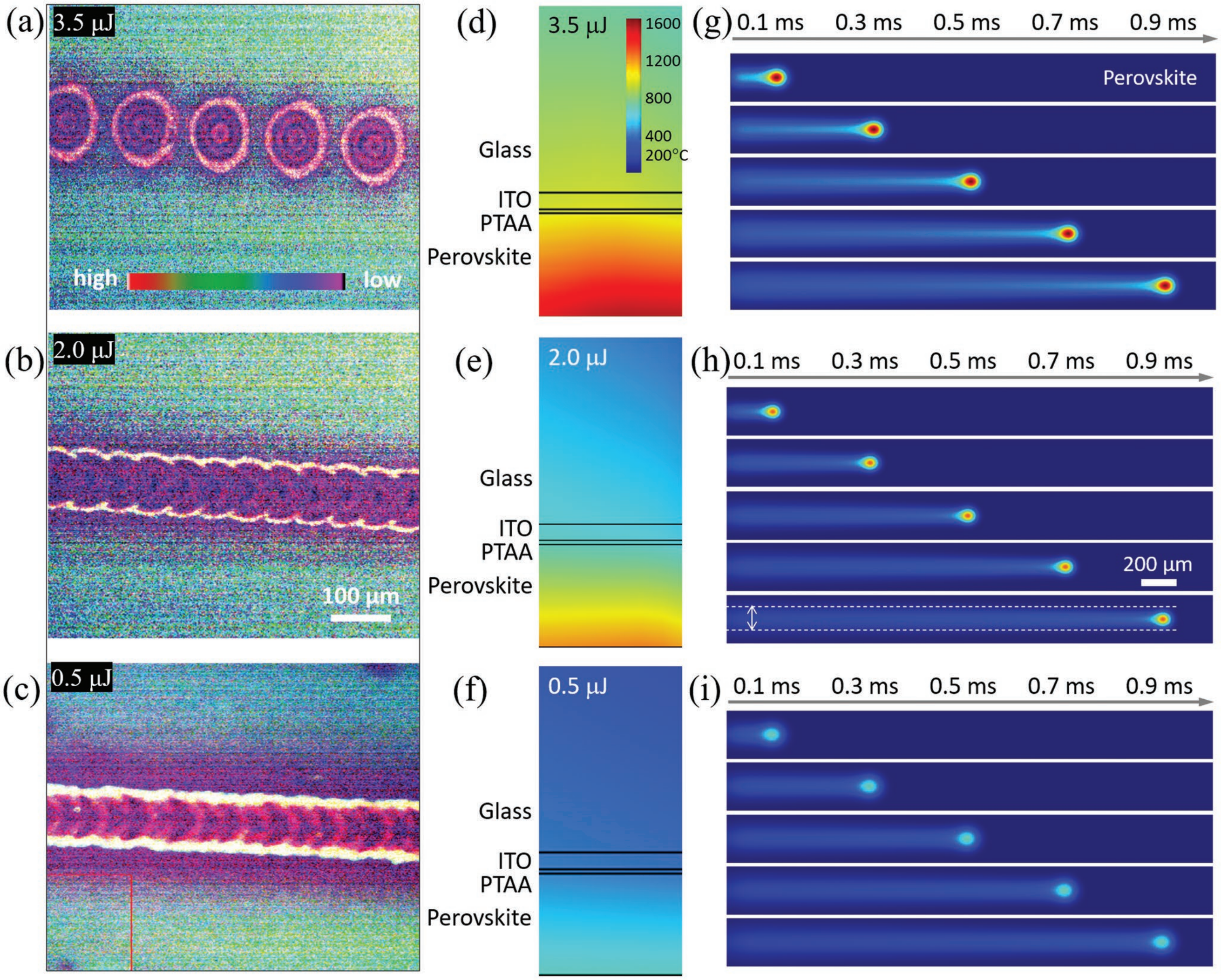

Figure 3. a–c) Photoluminescence mapping images of the P2 scribe line at different E_p; d–f) Simulated temperature profiles of cross-sections of laser spots with different pulse powers by using Comsol multiphysics-RF module. g–i) Simulation of temperature evolution by using Comsol multiphysics-RF module with different pulse powers.

for independent certification. The certified aperture area (12.84 cm^2) PCE under AM1.5G 100 mW cm^{-2} illumination under reverse scan (V_{OC} to I_{SC}) was 21.07%, with an I_{SC} of 46.86 mA, V_{OC} of 7.2 V, and FF of 80.22%. The PCE measured here is a record value for single junction PSMs reported thus far (Figure 4h,j and Figure S13, Supporting Information). The PCE obtained from the forward scan (I_{SC} to V_{OC}) is 20.31% with an I_{SC} of 47.32 mA, V_{OC} of 7.174 V, and FF of 76.81% (Figure S15, Supporting Information). This PSM exhibits a relatively small hysteresis index of 3.6%, which is no different from the PSC. More importantly, the champion PSM was also certified to have a constant output PCE of 20.10% over 300 s at the maximum power point (MPP) (Figure 4i and Figure S16, Supporting Information). Electroluminescence is a common method to characterize the defects in the module.[28] As can be seen in Figure 4f, the module exhibits an overall bright luminescence at a forward bias of 6.8 V, indicating that the perovskite thin film in the active area is uniform and that the interconnection quality in the dead areas is high. There is almost no efficiency loss when upscaling the device's active area from 0.09 to 12.26 cm^2 (22.16% vs 22.06%), and the GFF is as high as 95.5%, which is why the CTM efficiency loss in this work is limited to 1.09%.

3. Conclusions

In summary, efficient PSMs were fabricated using selective nanosecond-pulse laser-induced ablation. We show that the HAZ-P2 of the perovskite thin film is mostly determined by the spatial power profile of the laser rather than by the pulse duration, due to the small D_t of perovskite material, leading to a negligible TPD. The width of the HAZ-P2 and the HAZ-P3 can be optimized to just a few microns, contributing to the achievement of precise laser scribing and high GFF for the modules. Therefore, nanosecond laser is good enough to achieve the high-quality interconnection for perovskite solar modules. Micro-Raman spectroscopy was performed to identify the type and amount of residue within the scribes, and

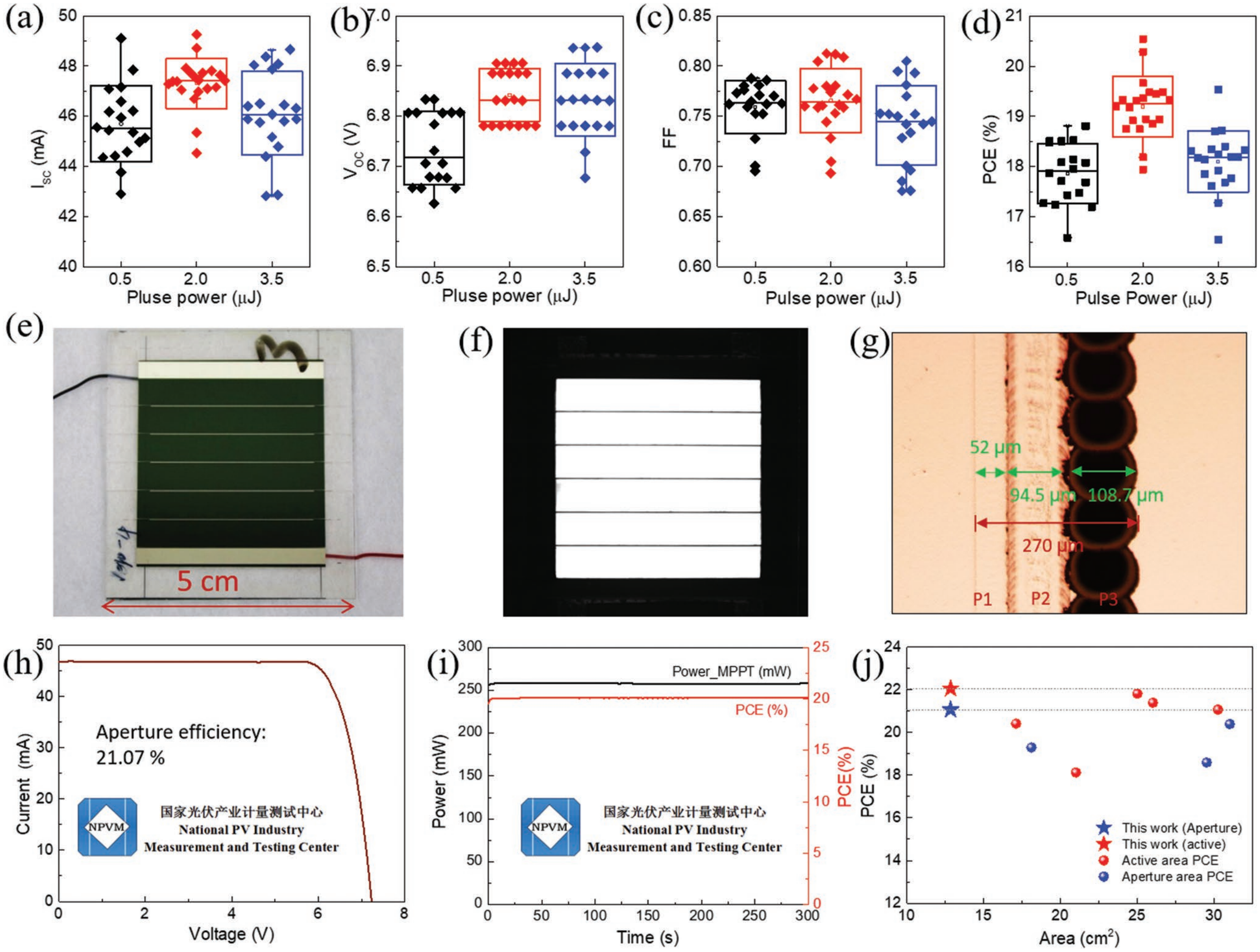

Figure 4. a–d) Statistics of I_{SC}, V_{OC}, FF, and PCE for PSMs fabricated at different E_p of the P2 scribe line, represented for 20 data points in each condition. e) Photograph of the PSM in this study. f) Electroluminescence image of the corresponding PSM at a forward bias of 6.8 V. g) Microscope image of the P1, P2, and P3 scribe lines in the dead area. h,i) The I–V curve under reverse scan and the maximum power point tracking curves certified by the Chinese national PV industry measurement and testing center (NPVM), under AM1.5G 100 mW cm^{-2} irradiation. j) The PCEs of PSMs as a function of the aperture (red) or active (blue) area of the module in this work and various modules in recent representative reports.[9–11,21–25]

photoluminescence mapping was used to identify the HAZ-P2. These characterizations were used as guidance to select the laser pulse power (E_p) to achieve optimized sub-cell interconnection quality and GFF. As a result, the champion PSM yielded a certified aperture efficiency of 21.07% and a GFF of 95.5%, which is one of the highest reported so far. This result leads the way to further simplification and reliability in PSM production.

4. Experimental Section

Materials: Lead iodide (PbI_2, purity >99.99%), cesium iodide (CsI, purity >99.9%), methylamine bromide (MABr, purity ≥99.5%), poly[bis(4-phenyl)(2,4,6-trimethylphenyl)amine (PTAA, purity ≥99.5%), C_{60} (purity ≥99.5%), 2-phenylethanamine iodide (PEAI, purity ≥99.5%), and lead bromide ($PbBr_2$, purity >99.99%), were purchased from Xi'an Polymer Light Co., Ltd. Formamidinium iodide (FAI, purity ≥99.99%) was purchased from Greatcell. Dimethyl sulfoxide (DMSO, purity ≥99.9%), *N*,*N*-dimethylformamide (DMF, purity ≥99.8%), chlorobenzene (purity ≥99%), and propan-2-ol (IPA, purity ≥99.5%) were purchased from Sigma-Aldrich.

Precursor Solution Preparation: The perovskite precursor solution of $Cs_{0.05}(FA_{0.9}MA_{0.1})_{0.95}Pb(I_{0.9}Br_{0.1})_3$ was prepared by mixing solutions of $FAPbI_3$, $MAPbBr_3$, and CsI in a volume ratio of 52:8:3. $FAPbI_3$ solution was prepared by adding 691.5 mg PbI_2 and 237.3 mg FAI into 1 mL DMF and DMSO (volume ratio is 4:1) mixture solvent, $MAPbBr_3$ solution was prepared by mixing 16.5 mg $PbBr_2$ and 46.35 mg MABr into 300 µL DMF and DMSO (volume ratio is 4:1) mixture solvent, and CsI solution was prepared by adding 58.5 mg CsI into 150 µL DMSO solvent.

Thin Film Deposition and Device Fabrication: The ITO-coated glass as substrate was washed in an ultrasonic bath where the order of washing medium was detergent (2 vol% Hellmanex III), deionized water, and ethanol, respectively. Each step lasted 15 min, and the substrates were further treated for 15 min in ultraviolet ozone after drying by N_2 flow. PTAA dissolved in chlorobenzene (1.5 mg mL^{-1}) was coated onto ITO at 4000 rpm for 30 s and then heated at 100 °C for 10 min to prepare the hole transport layer. Subsequently, Al_2O_3 nanoparticle solution (the original solution was diluted 1:50 in IPA) was deposited onto PTAA by spin coating at 4000 rpm for 30 s. To prepare the solar cell (substrate size: 2.5 × 2.5 cm), the perovskite solution was spin-coated with a two-step procedure at 2000 rpm for 3s and 4000 rpm for 35 s, respectively.

During the second step, 100 μL of ethyl acetate was dropped onto the spinning substrate 10 s prior to the end of the step. Then, the film was annealed at 120 °C for 20 min. For module (substrate size: 5 × 5.6 cm) fabrication, the same spin coating procedure was used, using 350 μL precursor ink and 300 μL ethyl acetate. After the deposition of the perovskite layer, the C_{60} film was evaporated to a thickness of 40 nm, and SnO_2 film was deposited by atomic layer deposition for 30 nm. Finally, the Ag electrode was thermally evaporated to a thickness of 120 nm.

Laser Scribing Procedure: The temperature was 24 ± 2 °C and the humidity was 45 ± 5% RH during the laser processing. The P1 isolation lines were scribed by the Helios fiber laser processing system at a wavelength of 1064 nm and minimal pulse duration of 30 ns. The P2 and P3 both were ablated by Helios VIS laser with a wavelength of 532 nm and minimal pulse duration of 0.4 ns. The average power was 3 W and the frequency was 70 kHz. The laser pulse energy was adjusted by rotating the polaroid without changing any optical path.

Characterization: The *I–V* characteristics of solar cells or modules were recorded in the air, using a Keithley 2400 source meter under standard light irradiance (AM1.5G, 100 mW cm^{-2}) as produced by a solar simulator (Newport, ORIEL-SOI3A). The PSCs and modules were unencapsulated during the test. For the PSCs, both forward and reverse scans were measured with a scanning speed of 0.15 V s^{-1}. For the PSMs, the scan speed was 0.5 V s^{-1}. The illumination area was 0.09 cm^2 for the PSCs, which was adjusted by a metal mask, and the illumination area was 12.96 cm^2 for the PSMs, in which, the area was adjusted by laser scribing lines. An anti-reflection film was used for the certified PSM. The EQE spectra were measured in DC mode on a spectrum corresponding system (Enlitech QE-R), calibrated by Si reference solar cell. All SEM images were scanned by FEI Apreo LoVac. The energy dispersive spectrometer (EDS) of FEI Apreo LoVac gave out the line element distribution information. Raman spectra were determined by using a Laser Raman co-focal micro spectrometry (HORIBA, XpoloRA PLUS) with a pixel size of 1 μm. XPS was performed by PHI 5000 VersaProbe III with a monochromatic Al Kα X-ray source with an X-ray beam size of 200 um. Charge compensation was achieved by the dual beam charge neutralization and the binding energy was corrected by setting the binding energy of the hydrocarbon C 1s feature to 284.8 eV. Electron probe microanalysis (EPMA) images were scanned by using an Electron Probe Microanalyzer (Shimadzu, EPMA-1720H). 3D micrographics were tested by white light 3d microscope (Leica DCM8 confocal mode with a resolution ratio of 0.1 nm, and Rtec UP-Sigma with a resolution ratio of 0.1 μm).

Supporting Information

Supporting Information is available from the Wiley Online Library or from the author.

Acknowledgements

Y.G. and C.L. contributed equally to this work. This work was supported by the National Natural Science Foundation of China (62005099, 62104082), Guangdong Basic and Applied Basic Research Foundation (2021B1515120003, 2022A1515010746, 2022A1515011228), and the Fundamental Research Funds for the Central Universities (21621024).

Conflict of Interest

The authors declare no conflict of interest.

Data Availability Statement

The data that support the findings of this study are available from the corresponding author upon reasonable request.

Keywords

aperture area efficiency, geometric filling factor, heat-affected zones, perovskite solar modules

Received: July 7, 2022
Revised: August 15, 2022

[1] A. Kojima, K. Teshima, Y. Shirai, T. Miyasaka, *J. Am. Chem. Soc.* **2009**, *131*, 6050.
[2] J. Jeong, M. Kim, J. Seo, H. Lu, P. Ahlawat, A. Mishra, Y. Yang, M. A. Hope, F. T. Eickemeyer, M. Kim, Y. J. Yoon, I. W. Choi, B. P. Darwich, S. J. Choi, Y. Jo, J. H. Lee, B. Walker, S. M. Zakeeruddin, L. Emsley, U. Rothlisberger, A. Hagfeldt, D. S. Kim, M. Grãtzel, J. Y. Kim, *Nature* **2021**, *592*, 381.
[3] H. Min, Do. Y Lee, J. Kim, G. Kim, K. Su Lee, J. Kim, M. J. Paik, Y. Ki Kim, K. S. Kim, M. G. Kim, T. J. Shin, S. I. Seok, *Nature* **2021**, *598*, 444.
[4] Best Research-Cell Efficiency Chart; https://www.nrel.gov/pv/cell-efficiency.html (accessed: August 2022).
[5] K. G. Brooks, M. K. Nazeeruddin, *Adv. Energy Mater.* **2021**, *11*, 2101149.
[6] B. Stegemann, C. Schultz, *Digital Encyclopedia Appl. Phys.* **2019**, https://doi.org/10.1002/3527600434.eap830.
[7] K. Xiao, Y.-H. Lin, M. Zhang, R. D. J. Oliver, Xi Wang, Z. Liu, X. Luo, J. Li, D. Lai, H. Luo, R. Lin, J. Xu, Yi Hou, H. J. Snaith, H. Tan, *Science* **2022**, *376*, 762.
[8] S. Moon, J. Yum, L. Löfgren, A. Walter, L. Sansonnens, M. Benkhaira, S. Nicolay, J. Bailat, C. Ballif, *IEEE J. Photovoltaics* **2015**, *5*, 1087.
[9] T. Bu, J. Li, H. Li, C. Tian, J. Su, G. Tong, L. K. Ono, C. Wang, Z. Lin, N. Chai, X-Li Zhang, J. Chang, J. Lu, J. Zhong, W. Huang, Y. Qi, Yi-B Cheng, F. Huang, *Science* **2021**, *372*, 1327.
[10] C. Liu, Y. Yang, K. Rakstys, A. Mahata, M. Franckevicius, E. Mosconi, R. Skackauskaite, B. Ding, K. G. Brooks, O. J. Usiobo, J.-N. Audinot, H. Kanda, S. Driukas, G. Kavaliauskaite, V. Gulbinas, M. Dessimoz, V. Getautis, F. De Angelis, Y. Ding, S. Dai, P. J. Dyson, M. K. Nazeeruddin, *Nat. Commun.* **2021**, *12*, 6394.
[11] J. W. Yoo, J. Jang, U. Kim, Y. Lee, S.-G. Ji, E. Noh, S. Hong, M. Choi, S. I. Seok, *Joule* **2021**, *5*, 2420.
[12] D. B. Ritzer, T. Abzieher, A. Basibüyük, T. Feeney, F. Laufer, S. Ternes, B. S. Richards, S. Bergfeld, U. W. Paetzold, *Prog. Photovolt.: Res. Appl.* **2022**, *30*, 360.
[13] C. L. Molpeceres, M. Colina, M. Holgado, M. Morales, I. Sanchez-Aniorte, S. Lauzurica, J. J. Garcia-Ballesteros, J. L Ocaña, *Laser-based Micro-and Nanopackaging and Assembly III. SPIE*, **2009**, *7202*, 260.
[14] N.-G. Park, K. Zhu, *Nat. Rev. Mater.* **2020**, *5*, 333.
[15] C. Liu, W. Li, H. Li, H. Wang, C. Zhang, Y. Yang, X. Gao, Q. Xue, H.-L. Yip, J. Fan, R. E. I. Schropp, Y. Mai, *Adv. Energy Mater.* **2019**, *9*, 1803572.
[16] C. Quarti, G. Grancini, E. Mosconi, P. Bruno, J. M. Ball, M. M. Lee, H. J. Snaith, A. Petrozza, F. De Angelis, *J. Phys. Chem. Lett.* **2013**, *5*, 279.
[17] T. Haeger, R. Heiderhoff, T. Riedl, *J. Mater. Chem. C* **2020**, *8*, 14289.
[18] X. Du, J. Li, G. Niu, J.-H. Yuan, K.-H. Xue, M. Xia, W. Pan, X. Yang, B. Zhu, J. Tang, *Nat. Commun.* **2021**, *12*, 3348.
[19] B. Baird, T. Gerke, K. Wieland, N. Paudel, *Proc. 26th European Photovoltaic Solar Energy Conference and Exhibition*, Hamburg, Germany, EU PVSEC, **2011**, pp. 2471–2474.
[20] L. A. Frolova, S. Y. Luchkin, Y. Lekina, L. G. Gutsev, S. A. Tsarev, I. S. Zhidkov, E. Z. Kurmaev, Z. X. Shen, K. J. Stevenson, S. M. Aldoshin, P. A. Troshin, *Adv. Energy Mater.* **2021**, *11*, 2002934.

[21] M. Jeong, I. W. Choi, K. Yim, S. Jeong, M. Kim, S. J. Choi, Y. Cho, J.-H. An, H.-B. Kim, Y. Jo, S.-H. Kang, J.-H. Bae, C.-W. Lee, D. S. Kim, C. Yang, *Nat. Photonics* **2022**, *16*, 119.

[22] X. Liu, M. Chen, Yi Zhang, J. Xia, J. Yin, Mo Li, K. G. Brooks, R. Hu, X. Gao, Y.-H. Kim, A. Züttel, J M. Luther, S. Kinge, Y. Feng, M. K. Nazeeruddin, *Chem. Eng. J.* **2022**, *431*, 133713.

[23] J. Li, H. Wang, X. Y. Chin, H. A. Dewi, K. Vergeer, T. W. Goh, J. W. M. Lim, J. H. Lew, K. P. Loh, C. Soci, T. C. Sum, H. J. Bolink, N. Mathews, S. Mhaisalkar, A. Bruno, *Joule* **2020**, *4*, 1035.

[24] S. Chen, X. Dai, S. Xu, H. Jiao, L. Zhao, J. Huang, *Science* **2021**, *373*, 902.

[25] Y. Deng, S. Xu, S. Chen, X. Xiao, J. Zhao, J. Huang, *Nat. Energy* **2021**, *6*, 633.

[26] P. Mialhe, A. Khoury, J. Charles, *Phys. Status Solidi A* **1984**, *83*, 403.

[27] D. S. Chan, J. C. Phang, *IEEE Trans. Electron Devices* **1984**, *31*, 381.

[28] A. Gerber, V. Huhn, T. Tran, M. Siegloch, Y. Augarten, B. Pieters, U. Rau, *Sol. Energy Mater. Sol. Cells* **2015**, *135*, 35.